

Fast Range Decoupling Algorithm for Metamaterial Aperture Real-time Imaging

Yuteng Gao¹, Wencan Peng², Min Wang³, Chenjiang Guo¹, and Jun Ding¹

¹ School of Electronics and Information, Northwestern Polytechnical University, Xi'an, 710129, China
ytgao2002@163.com, cjguo@nwpu.edu.cn, dingjun@nwpu.edu.cn

² Xi'an Institute of Space Radio Technology, (CASC, Xi'an), Xi'an, 710100, China
wcanpeng@163.com

³ National Lab of Radar Signal Processing, Xidian University, Xi'an, 710071, China
wangmin@xidian.edu.cn

Abstract — While metamaterial aperture imaging systems do not require mechanical scanning equipment or complex components by employing a spatially variant radiation field, they require large amount of data and many computations. In this paper, we deduce the contribution of the resonator to the radiation fields of the metamaterial aperture. We propose a fast range decoupling algorithm that can improve the data processing speed and obtain real-time images of far-field scenes. The algorithm decomposes the scene into numerous range cells, drastically reduces the range of interest, and reconstructs the scene in parallel. Simulation results show that computational cost is significantly decreased and image quality is maintained.

Index Terms — millimeter-wave imaging, metamaterial apertures, compressed sensing, decoupling

I. INTRODUCTION

Millimeter-wave imaging techniques can provide high-quality imagery with nonionizing radiation and are promising in a variety of applications, such as medical diagnosis [1], bio-imaging [2], security screening [3] and through-the-wall imaging [4],[5]. Conventional millimeter-wave imaging systems usually rely on mechanical equipment to scan a static aperture. Phased arrays can generate different imaging models without mechanical scanning, yet they need many phase shifts, attenuators and other components which results in increased cost and size. In recent research, frequency-diverse aperture imaging has been shown to be a possible solution to the above problems. By generating a group of different spatial radiation fields that change rapidly with frequency, the frequency-diverse aperture antenna can encode the scene information. Many frequency-diverse antenna architectures have been demonstrated, such as metamaterial apertures [6]-[11], cavity apertures [12]-[14], and dynamic metasurface apertures [15]-[18].

Compared with dynamic metasurface apertures and cavity apertures, metamaterial apertures have the advantages of simple structure and low cost.

Although simple and inexpensive, metamaterial apertures also have flaws. First, a metamaterial aperture antenna is not easy to design, especially for millimeter wave imaging applications. The radiation patterns change with respect to frequency, and cannot be predicted in an exact way. Since Hunt et al. [6] first used waveguide-fed metamaterial apertures that consist of complementary electric-field-coupled (cELC) elements in imaging experiments, many studies have focused on new structures of metamaterial apertures. To obtain a uniform excitation, Guy [10] designed a sparse aperture in which they removed elements randomly. Na [19] designed apertures with cELC and complementary Jerusalem cross (CJC) units to raise radiation efficiency. In [20], Zhao designed a bunching metamaterial antenna that could generate frequency-diverse bunching random radiation pattern. In these literatures, cELC elements and other units were distributed randomly, and entire designs relied on the full-wave electromagnetic simulation. Some traditional modeling methods could also be used for metamaterial aperture modeling and designing, such as fast multipole method (FMM) [21], series expansion method [22], and boundary element method (BEM) method [23]. Recently years, some new technics have been developed in electromagnetic modeling. In [24], a full-wave finite-element-based method was introduced. Feng [25] used combined neural networks for parametric modeling of electromagnetic (EM) behavior of microwave components. Calik [26] proposed a fully-connected regression model based on Bayesian optimization for frequency selective surfaces. These methods could be considered in the design of the metamaterial apertures antenna. Second, in the metamaterial aperture imaging model, discretization of the whole imaging zone will inevitably result in the

particularly high dimensionality of the measurement matrix and the huge computational cost in further imaging processing. In order to get real-time images, reducing the scale of the inverse problem is necessary. A feasible approach is to constrain the imaging volume and thus decrease the corresponding number of discretization voxels. It is mentioned in [27] that the Microsoft Kinect sensor working at infrared wavelength can potentially be used for reducing reconstruction volume, whereas this approach would be problematic if the targets span across many far different range bins. To enhance the capability of the system, multi-GPU parallel processing architectures were studied in [28]. In traditional SAR imaging, there is coupling between the range dimension and azimuth dimension. The range-Doppler (RD) algorithm [29] decomposes the coupling two-dimensional scene focusing problem into two one-dimensional focusing problems, which is also the most popular decoupling method. In [30], a range decoupling method was applied in metamaterial aperture imaging to reduce the dimensionality of the measurement matrix and accelerate computation, but the running time still could not be neglected.

In this work, we deduce the contribution of the cELC resonator to the radiation fields of the metamaterial aperture, and propose a fast range decoupling method for metamaterial aperture-based imaging systems. The algorithm allows the scene to be decomposed into a set of range cells, the range of interest to be drastically reduced according to the IFFT results, and the scene to be reconstructed in a parallel way. Compared with the conventional approach, the proposed algorithm requires less computational cost and running time, and produces real-time images. Multiple simulations verify the effectiveness of the proposed algorithm.

The rest of this paper is structured as follow. In Section II, we briefly introduce the general forward metamaterial imaging model. Section III deduces the contribution of the cELC resonator to the radiation fields of the metamaterial aperture, and discusses the character of the measurement matrix. Section IV devotes the derivation fast range decoupling approach. In section V, we present the imaging simulation to demonstrate the effectiveness of the proposed method. Conclusions are presented in Section VI.

II. MATHEMATICAL IMAGING MODEL

The mathematical model of the metamaterial aperture forward imaging system will be introduced in this section. As shown in Fig. 1, a dielectric-filled parallel-plate waveguide is employed as the transmitter. An array of subwavelength cELC elements with different physical geometries are randomly distributed on the upper plane of the waveguide. Different subsets of elements are excited with changing frequency. Backscatters from the objects in the scenes are received by an open-ended waveguide probe, which is on the antenna plane and

close to the transmitter plane. The vector $\mathbf{r} = (x, y, 0)$ represents the points on the metamaterial aperture antenna, which is on the reference plane, and the vector $\mathbf{r}' = (x', y', z')$ indicates the points in the imaging scene.

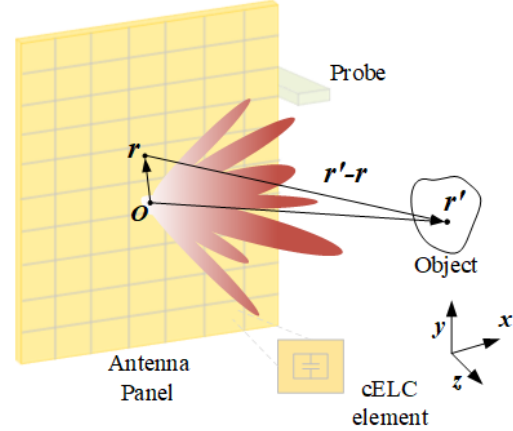


Fig. 1. Panel to probe imaging system.

Suppose $T_{tx}(\mathbf{r})$ is the antenna impulse response. The field in the reference plane could also be illustrated by this response. According the Helmholtz equation, the field in the imaging scene can be given as:

$$U_{oTX}(\mathbf{r}') = \int_{\text{scene}} T(\mathbf{r}) \frac{\partial}{\partial z} G(\mathbf{r}', \mathbf{r}) d^2\mathbf{r}, \quad (1)$$

where

$$G(\mathbf{r}', \mathbf{r}) = \frac{\exp(-jk_0 |\mathbf{r}' - \mathbf{r}|)}{4\pi |\mathbf{r}' - \mathbf{r}|}, \quad (2)$$

is Green's function, which describes the solution for impulse response from a source in free space. Taking z as the propagation axis, $(\partial / \partial z)G(\mathbf{r}', \mathbf{r})$ represents the scalar field propagator from the location \mathbf{r} on the reference plane to the location \mathbf{r}' on a parallel plane in imaging scene [30]. k_0 is the wavenumber, given as $k_0 = 2\pi f / c$, where f denotes the spatial frequency and c denotes the speed of light.

Assuming that the incident radiation field irradiates the scene target and the target scatters the incident electromagnetic wave. $U_s(\mathbf{r}')$ is used to represent the target scattering field, and the total field of the imaging scene can be obtained as follows:

$$U_{To}(\mathbf{r}') = U_{oTX}(\mathbf{r}') + U_s(\mathbf{r}'). \quad (3)$$

The wave equation in the case of uniform medium scattering is expressed as:

$$\nabla^2 U_{To}(\mathbf{r}') + k(\mathbf{r}')^2 U_{To}(\mathbf{r}') = 0, \quad (4)$$

where

$$k(\mathbf{r}') = k_0 n(\mathbf{r}') = k_0 [1 + n_s(\mathbf{r}')], \quad (5)$$

is the refractive index of the scattering medium, and

$$n_s(\mathbf{r}') = [\mu(\mathbf{r}')\varepsilon(\mathbf{r}') / \mu_0\varepsilon_0]^{1/2}.$$

Considering that the incident radiation field $U_{oTX}(\mathbf{r}')$ must satisfy the Helmholtz equation, it can be obtained:

$$\nabla^2 U_{oTX}(\mathbf{r}') + k_0^2 U_{oTX}(\mathbf{r}') = 0. \quad (6)$$

Substituting (5) and (6) into (4), the target scattering field $U_s(\mathbf{r}')$ can be written as:

$$\nabla^2 U_s(\mathbf{r}') + k_0^2 U_s(\mathbf{r}') = -(k(\mathbf{r}')^2 - k_0^2) U_{To}(\mathbf{r}'). \quad (7)$$

It should be noted that there is a nonlinear relationship between the scattering field and the target scatter function. Without any approximate treatment of the scattering field, the upper differential equation cannot be solved. In this section, the first order Born approximation assumption is used to ignore the second-order terms [31]. Then, the Helmholtz equation could be represented as:

$$\nabla^2 U_s(\mathbf{r}') + k_0^2 U_s(\mathbf{r}') = -\sigma(\mathbf{r}') U_{To}(\mathbf{r}'), \quad (8)$$

where

$$\sigma(\mathbf{r}') = 2k_0 n_s(\mathbf{r}'), \quad (9)$$

donates the reflectivity of scene target.

Treating the scene as the radiation source, the source-field propagation Green's function is used to solve the above equation. In this case, the scattering field at the transmit aperture (reference plane) $U_s(\mathbf{r}')$ is represented as:

$$U_s(\mathbf{r}') = \int_V -G(\mathbf{r}, \mathbf{r}') \sigma(\mathbf{r}') U_{To}(\mathbf{r}') d^3 \mathbf{r}'. \quad (10)$$

Considering the effect of weak perturbation from the scattered field on the total field $U_{To}(\mathbf{r}')$, we can rewrite (10) as:

$$U_s(\mathbf{r}') = \int_V -G(\mathbf{r}, \mathbf{r}') \sigma(\mathbf{r}') U_{oTX}(\mathbf{r}') d^3 \mathbf{r}'. \quad (11)$$

Revisiting (2), we obtain the relationship between the derivative of Green's function $(\partial / \partial z)G(\mathbf{r}', \mathbf{r})$ and the Green's function G yield itself [32]:

$$\frac{\partial}{\partial z} G(\mathbf{r}, \mathbf{r}') = \cos(\mathbf{z}, \mathbf{r}_p) \left(jk_0 - \frac{1}{|\mathbf{r}_p|} \right) G(\mathbf{r}, \mathbf{r}'), \quad (12)$$

where $\cos(\mathbf{z}, \mathbf{r}_p)$ denotes the cosine of the angle between \mathbf{z} and \mathbf{r}_p joining \mathbf{r} to \mathbf{r}' . Assuming that the field of view (FOV) is narrow, we can simplify the above equation as:

$$\frac{\partial}{\partial z} G \approx jk_0 G. \quad (13)$$

Therefore, the scattering field at the transmit aperture $U_s(\mathbf{r}')$ can be represented as:

$$U_s(\mathbf{r}') = -\frac{1}{jk_0} \int_V \sigma(\mathbf{r}') U_{oTX}(\mathbf{r}') \frac{\partial}{\partial z} G(\mathbf{r}, \mathbf{r}') d^3 \mathbf{r}'. \quad (14)$$

Assume that the receiving probe antenna is located at the same plane as the transmitting metamaterial aperture antenna, and the pulse response is $T_{rx}(\mathbf{r})$. Since

the scattering field on the receiving aperture is known, the measured value g of the receiving probe antenna can be calculated as [33]:

$$g = \int_S T_{rx} U_s(\mathbf{r}') d^2 \mathbf{r}. \quad (15)$$

Substituting (12) and (14) into (15), g can be rewritten as:

$$g = \int_V U_{oTX}(\mathbf{r}') U_{oRX}(\mathbf{r}') \sigma(\mathbf{r}') d^3 \mathbf{r}, \quad (16)$$

where $U_{oRX}(\mathbf{r}')$ represents the field produced by the receiving probe antenna at location \mathbf{r} .

Considering that the metamaterial aperture antenna can generate frequency-diverse random radiation fields to detect the scene, a set of measurement echo vectors indexed by frequency can be calculated as:

$$\mathbf{g}(f) = \int_V U_{oTX}(\mathbf{r}', f) U_{oRX}(\mathbf{r}', f) \sigma(\mathbf{r}') d^3 \mathbf{r}. \quad (17)$$

Assuming the reflectivity of objects in scene is isotropic, since the imaging resolution is limited by the antenna aperture, the scene can be decomposed to 3D discrete voxels and encoded by a finite number of frequency diverse models. Then (17) can be rewritten as a finite-dimensional matrix equation:

$$\mathbf{g} = \mathbf{H}\boldsymbol{\sigma} + \mathbf{n}, \quad (18)$$

where \mathbf{g} denotes the $M \times 1$ measurement vector, \mathbf{n} is an $M \times 1$ noise vector, $\boldsymbol{\sigma}$ is the $N \times 1$ scattering coefficient vector across N pixels of the imaging scene, and \mathbf{H} denotes the $M \times N$ measurement matrix, which is the dot product of the incident and scattered fields. The above equation clearly describes the receiving and processing of scattering electromagnetic waves in the scene.

In order to get a unique linear solution for the scattering information $\boldsymbol{\sigma}$ in the scene, the rank of \mathbf{H} must equal the dimension of $\boldsymbol{\sigma}$. In another word, $M = N$. However, in the application of imaging scenarios, the rank of \mathbf{H} is much less than the dimension of scattering coefficient $\boldsymbol{\sigma}$. According the compress sensing theory, the underdetermined scenes could be reconstructed by solving the optimization problem:

$$\boldsymbol{\sigma}_{\text{est}} = \arg \min_{\boldsymbol{\sigma}} \|\mathbf{g} - \mathbf{H}\boldsymbol{\sigma}\|_2^2 + \gamma \|\boldsymbol{\sigma}\|_1, \quad (19)$$

where γ is the regularization parameter.

Numerous algorithms exist for solving this optimization problem, such as greedy algorithm, convex optimization algorithm and Bayesian algorithm. Here we use the orthogonal matching pursuit (OMP) algorithm, which is a classic greedy algorithm, to solve this problem. The ensemble measurement matrix is used directly during this processing, which is called brute force method. Since $M \ll N$, the brute force method needs amount of computational cost and relative long running time. In order to get new algorithms which could accelerate the calculation, we will analysis the measurement matrix in following section.

III. APERTURE MODEL AND MEASUREMENT MATRIX CHARACTER

For the frequency-diverse metamaterial aperture employed in our imaging system, the field pattern \mathbf{T} consists of a relatively random set of nulls and lobes that change with frequency. At a given angle, the magnitudes and phase of the field vary irregularly over the bandwidth. The frequency diverse radiation field of the metamaterial aperture is generated by an array of cELC elements with various resonance frequencies. Generally, a cELC element can be modelled as a polarizable radiation magnetic dipole. The polarization of it can be described according to the Lorentzian dispersion:

$$\alpha(\omega) = -\frac{F\omega^2}{\omega^2 - \omega_0^2 + j\omega\gamma}, \quad (20)$$

where $\omega = 2\pi f$ is the angular frequency, ω_0 is the angular resonance frequency of the resonator, $\gamma = \omega_0 / 2Q$ is the damping factor, and F is proportional to the oscillator strength and coupling, which is assumed to be 1. The dipole moment of the dipole at location \mathbf{r} can be calculated as:

$$\mathbf{m}(\mathbf{r}, \omega) = \alpha(\mathbf{r}, \omega) \cdot U_G(\mathbf{r}, \omega), \quad (21)$$

where $U_G(\mathbf{r}, \omega)$ is the local guided field. Assuming that these dipoles are all y-polarized, the radiation pattern of location \mathbf{r}' from a dipole at location \mathbf{r} can be approximated as:

$$U(\mathbf{r}', \mathbf{r}, \omega) \approx \mathbf{m}(\mathbf{r}, \omega) \frac{Z_0 k_0}{4\pi R'} \exp(-jk_0 R') \sin \theta, \quad (22)$$

where R' is the distance between \mathbf{r}' and \mathbf{r} , Z_0 is the impedance of free space, and θ is the angle between \mathbf{r}' and $\mathbf{m}(\mathbf{r})$. Compared with the standard approximation for the far-field radiation of a dipole, we ignore all higher-order terms that vary as $1/R'^2$ or $1/R'^3$. The total transmit field at location \mathbf{r}' in the scene can be calculated by superposing radiation fields from all dipoles in the aperture:

$$U_{oTX}(\mathbf{r}', f) = U_{oTX}(\mathbf{r}', \omega) = \sum_{\mathbf{r}} U(\mathbf{r}', \mathbf{r}, \omega). \quad (23)$$

The above deduction shows that by sweeping frequency ω , the polarizability and local guided field of each dipole are changed, and then the dipole moment is modified. Moreover, the radiation fields of the resonator and entire array are affected. Hence the radiation fields of the metamaterial aperture change with respect to ω . ω serves as a parameter to index the measurement modes.

In the derivation of Section II, \mathbf{H} is the dot product of transmitting fields in the scene of the transmitting metamaterial aperture antenna and the receiving probe. In the far field, the distance from the metamaterial aperture antenna to location \mathbf{r}' and the distance from the receiving probe to location \mathbf{r}' can be approximately

equal. The relevant term $1/|\mathbf{r}' - \mathbf{r}|$ in the Green's function could be ignored. The transmitting field on \mathbf{r}' in the scene can be written as:

$$U_{oTX}(\mathbf{r}') = T e^{-jk_0 R}, \quad (24)$$

where R is the distance between the center of the transmitting aperture and position \mathbf{r}' in the scene, and T denotes the radiation field of the metamaterial aperture panel.

For convenient analysis, we ignore the radiation pattern from the open waveguide probe, and treat it as an omnidirectional receiving probe. The product of incident and scattering fields at position \mathbf{r}' in the scene (corresponding range R), can be expressed as:

$$\mathbf{h}_R = \mathbf{t} e^{-j2k_0 R} = \mathbf{t} e^{-j4\pi R/c}, \quad (25)$$

where \mathbf{t} and \mathbf{f} denote the radiation field pattern and the variational frequency, respectively. $e^{-j4\pi R/c}$ is the propagation factor and is a linear phase term related to R . It is obvious that \mathbf{h}_R is a column entry of measurement matrix \mathbf{H} , and \mathbf{H} can be expressed as:

$$\mathbf{H} = \mathbf{T} \mathbf{G}(\mathbf{r}', \mathbf{r}, \mathbf{f}) \quad (26)$$

Hence a row entry of \mathbf{H} is the product of the radiation field pattern \mathbf{T} and appropriate Green's function. When the frequency changes, a distinct spatial radiation pattern \mathbf{T} is generated by the metamaterial aperture and a new row entry of \mathbf{H} is obtained.

For a given metamaterial aperture antenna, the frequency sampling interval Δf needs to be determined. However, when we choose Δf , it is important to note that the maximum unambiguous range (MUR), represented by $c/2\Delta f$, is closely related to image quality, and Δf directly influences the frequency points. After determining Δf , the limited frequency bandwidth (named subband) B_Δ has to be ascertained. By the IFFT process for the radiation field within a proper B_Δ , we could get a sequence with a sinc-like magnitude distribution. Then, the limited frequency bandwidth B_Δ can be ascertained experimentally.

Table 1: Antenna parameters

Bandwidth	18.5~25GHz
Frequency sampling interval	8.125MHz
Field of view	-70°~70°
Azimuth sampling interval	0.5°
Panel length	0.4m
Dimension of \mathbf{T}	801×281

Here we employed measured radiation field data of the antenna from [6]. The parameters of antenna are listed in Table 1. The prototype is a 1D leaky waveguide, formed by patterning the top conductor of a standard microstrip line with cELC elements. This antenna could

explore 2D (range and azimuth) sparse scenes.

We randomly select an azimuth angle within the field of view. For the radiation fields \mathbf{t} at this angle within the subband B_Δ , the results of IFFT operation are shown in Fig. 2 (a). The magnitudes take the form of a sinc-like distribution. Recalling (20), the measurement vector \mathbf{h}_R is the product of the radiation fields \mathbf{t} and the propagation factor. This propagation factor, as a linear phase term related to R , corresponds to the shift of the sequence in the time domain, according to the frequency-shift property of the IFFT. The results of IFFT with respect to \mathbf{h}_R , which is calculated from \mathbf{t} , are also shown in Fig. 2 (a). We can find that the IFFT results of \mathbf{h}_R shift to the right compared to that of radiation field \mathbf{t} . The shift units represent range R corresponding to \mathbf{h}_R . This behavior would still exist if the IFFT is performed over entire bandwidth, as shown in Fig. 2 (b).

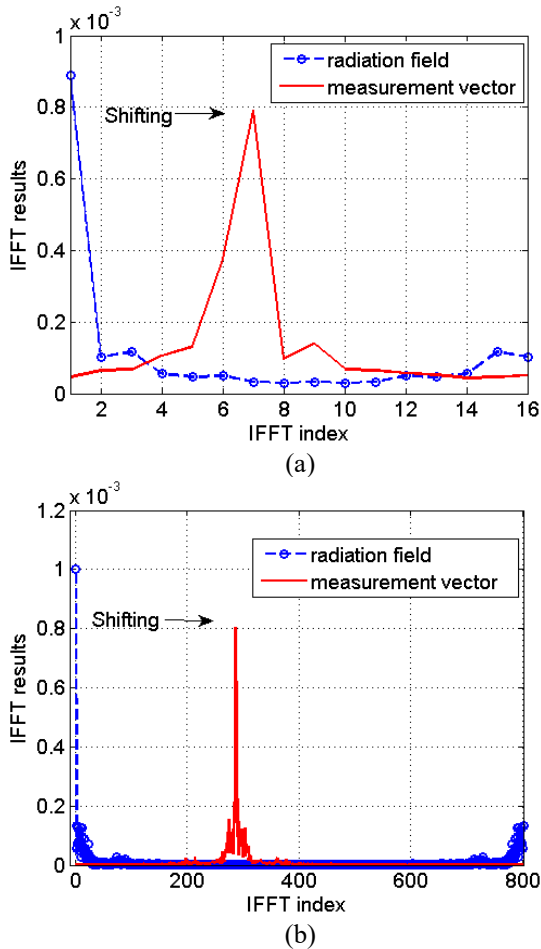


Fig. 2. IFFT results of radiation fields \mathbf{t} and the measurement vector \mathbf{h}_R .

Considering that the echo data measured by the receiving antenna are the product of \mathbf{h}_R and reflectivity of scatters, if we perform IFFT with respect to echo data

\mathbf{g} , the frequency-shift property still exists. Hence, we can deduce the approximate ROI according to the shift units of maxima and the range resolution corresponding to B_Δ . Since the resolution is inversely proportional to the bandwidth, if we perform IFFT with respect to \mathbf{g} over the entire working bandwidth, the detailed range position of scatters could be obtained, and the ROI would be reduced. This behavior will be verified in the simulation of a later section.

The above analysis focuses on arbitrarily chosen azimuth angle radiation fields within B_Δ . Now, we use a sliding window that has the same size as B_Δ to carry out IFFT operation on the entire bandwidth, while the shift length is one frequency point. The results of the sliding-windowed IFFT are shown in Fig. 3. It is obvious that the position of maxima barely moves. Hence the Sinc-like distributions remain on entire band. Considering that the azimuth angle is randomly chosen, this behavior is also suitable for the ensemble azimuth field, which is the foundation for the further deduction of our algorithm.

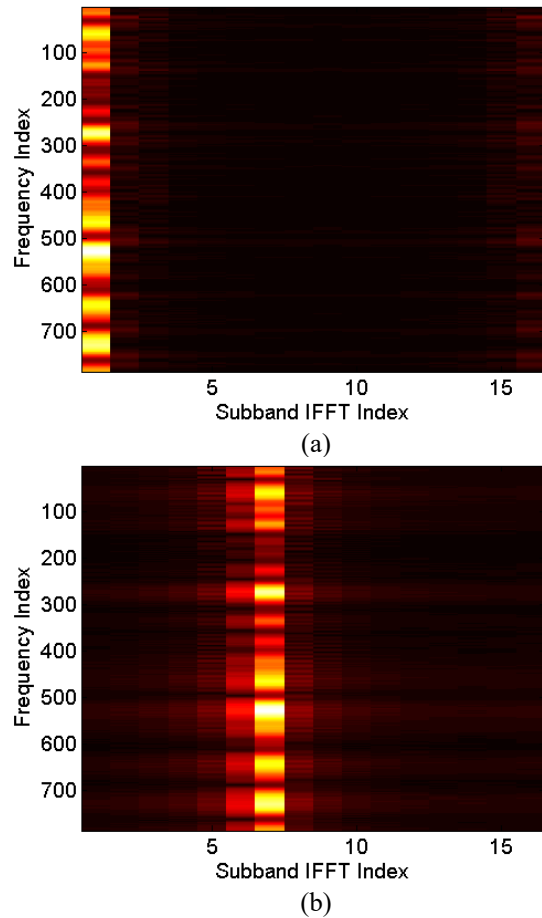


Fig. 3. Sliding-windowed IFFT results of (a) the azimuth fields, and (b) measurement vector over the entire frequency band.

In the above discussion, the targets contained in the imaging space are concentrated at the relatively close range bins. Then the reflectivity coefficients of the voxels outside the ROI are equal to 0. The measured echo data \mathbf{g} are purely the product of constrained \mathbf{H} and $\boldsymbol{\sigma}$ corresponding to the ROI. If we apply IFFT with respect to \mathbf{g} , the ROI can be obtained, and then $\boldsymbol{\sigma}$ can be retrieved with the constrained \mathbf{H} . However, if the targets contained in the imaging space span some far different range bins, this method will be intractable rapidly. This issue will be discussed in follow section.

IV. FAST RANGE DECOUPLING ALGORITHM

Let $\boldsymbol{\sigma}$ denote all reflection coefficients contained in the imaging scene, and $\mathbf{g}_\Delta \in \mathbb{C}^{P \times 1}$ denote P receiving measurements of the whole scene within subband B_Δ , which contains P frequency points. For an extracted range area \mathbf{R}_1 , the corresponding measurement matrix is $\mathbf{H}_{\mathbf{R}_1}$; then, the relative received frequency measurement can be represented as $\mathbf{g}_{\mathbf{R}_1} = \mathbf{H}_{\mathbf{R}_1} \boldsymbol{\sigma}_{\mathbf{R}_1}$, which constitutes a portion of \mathbf{g}_Δ . The IFFT results with respect to $\mathbf{g}_{\mathbf{R}_1}$ can be expressed as matrix equation

$$\boldsymbol{\psi} = \mathbf{D}_P \mathbf{g}_{\mathbf{R}_1}, \quad (27)$$

where $\boldsymbol{\psi}$ denotes the IFFT return and \mathbf{D}_P is the inverse discrete Fourier transform matrix, which can be written as:

$$\mathbf{D}_P = \frac{1}{P} \begin{bmatrix} 1 & 1 & 1 & \cdots & 1 \\ 1 & W_P^1 & W_P^2 & \cdots & W_P^{P-1} \\ 1 & W_P^2 & W_P^4 & \cdots & W_P^{2(P-1)} \\ \vdots & \vdots & \vdots & \ddots & \vdots \\ 1 & W_P^{P-1} & W_P^{2(P-1)} & \cdots & W_P^{(P-1)(P-1)} \end{bmatrix}, \quad (28)$$

where $W_P = \exp(j2\pi/P)$. Since $\mathbf{g}_{\mathbf{R}_1} = \mathbf{H}_{\mathbf{R}_1} \boldsymbol{\sigma}_{\mathbf{R}_1}$, $\boldsymbol{\psi}$ can be written as:

$$\boldsymbol{\psi} = \mathbf{D}_P \mathbf{H}_{\mathbf{R}_1} \boldsymbol{\sigma}_{\mathbf{R}_1} = \mathbf{D}_P \begin{bmatrix} \mathbf{h}_1 \\ \mathbf{h}_2 \\ \vdots \\ \mathbf{h}_p \end{bmatrix} \boldsymbol{\sigma}_{\mathbf{R}_1}. \quad (29)$$

Processing IFFT with respect to \mathbf{g} on all frequency points, we get the detailed range index of objects, and the corresponding area \mathbf{R}_2 , where $\mathbf{R}_2 \subset \mathbf{R}_1$. Since all the received waves corresponding to \mathbf{R}_1 are scattered by the objects in \mathbf{R}_2 , $\mathbf{g}_{\mathbf{R}_1}$ can be expressed as:

$$\mathbf{g}_{\mathbf{R}_1} = \mathbf{H}_{\mathbf{R}_1} \boldsymbol{\sigma}_{\mathbf{R}_1} = \mathbf{H}_{\mathbf{R}_2} \boldsymbol{\sigma}_{\mathbf{R}_2} \quad (30)$$

and $\boldsymbol{\psi}$ can be written as:

$$\boldsymbol{\psi} = \mathbf{D}_P \mathbf{H}_{\mathbf{R}_1} \boldsymbol{\sigma}_{\mathbf{R}_1} = \mathbf{D}_P \mathbf{H}_{\mathbf{R}_2} \boldsymbol{\sigma}_{\mathbf{R}_2} = \mathbf{D}_P \begin{bmatrix} \mathbf{h}_1 \\ \mathbf{h}_2 \\ \vdots \\ \mathbf{h}_p \end{bmatrix} \boldsymbol{\sigma}_{\mathbf{R}_2}. \quad (31)$$

For the case in Fig. 3, the corresponding maximum can be expressed as:

$$\psi_{\max} = \frac{1}{P} \begin{bmatrix} 1 & W_P^4 & \cdots & W_P^{4(P-1)} \end{bmatrix} \begin{bmatrix} \mathbf{h}_1 \\ \mathbf{h}_2 \\ \vdots \\ \mathbf{h}_p \end{bmatrix} \boldsymbol{\sigma}_{\mathbf{R}_2}. \quad (32)$$

Henceforth, the maximum ψ_{\max} can be considered as a new measurement $\boldsymbol{\psi}$. The inner product between the Fourier coefficient and original measurement matrix $\mathbf{H}_{\mathbf{R}_2}$, denoted by $\boldsymbol{\phi}$, is the new sensing vector.

In the above derivation, the measurement vector $\mathbf{g}_{\mathbf{R}_1}$ turns to a single measurement ψ_{\max} , and the measurement matrix $\mathbf{H}_{\mathbf{R}_1}$ turns to a sensor vector $\boldsymbol{\phi}$. We get a new measurement equation:

$$\boldsymbol{\psi} = \boldsymbol{\Phi} \boldsymbol{\sigma}. \quad (33)$$

The new measurement matrix is still underdetermined, so we can get reflection coefficients $\boldsymbol{\sigma}$ by solving an optimization problem:

$$\boldsymbol{\sigma}_{\text{est}} = \arg \min_{\boldsymbol{\sigma}} \|\boldsymbol{\Psi} - \boldsymbol{\Phi} \boldsymbol{\sigma}_{\text{est}}\|_2^2 + \gamma \|\boldsymbol{\sigma}_{\text{est}}\|_1. \quad (34)$$

Comparing (34) with (19), the dimension of the new measurement matrix $\boldsymbol{\Phi}$ is much less than the dimension of \mathbf{H} . If we use same algorithm, such as OMP, (34) would require less computational cost and running time.

If the targets are located in far more range cells in the scene, we can obtain multiple equations, and the above reconstruction can be performed in parallel.

Our proposed fast range decoupling algorithm can be summarized as follows:

Step 1. Initialize the received frequency measurements \mathbf{g} and radiation field \mathbf{T} .

Step 2. Confirm sub-bandwidth B_Δ from \mathbf{T} , and record the index of maximum column of the IFFT return.

Step 3. Process \mathbf{g} with sliding-window IFFT to ascertain the range region \mathbf{R}_1 that contains targets by the index of maxima. And record the corresponding new measurements $\boldsymbol{\Psi}$.

Step 4. Perform IFFT with respect to \mathbf{g} and confirm the range location \mathbf{R}_2 of targets according to the peak index of results.

Step 5. Build the new measurement matrix $\boldsymbol{\Phi}$ with respect to \mathbf{R}_2 , and get new measurement equation $\boldsymbol{\Psi} = \boldsymbol{\Phi} \boldsymbol{\sigma}_{\mathbf{R}_2}$.

Step 6. Reconstruct $\boldsymbol{\sigma}_{\mathbf{R}_2}$ from the measurement

equation and rebuild the ensemble σ .

V. SIMULATIONS AND ANALYSIS

In this section, the imaging capabilities of the proposed fast range decoupling algorithm are demonstrated. Radiation field data of the measured antenna are employed in multiple imaging simulations. The parameter of antenna is listed in Table 1.

The azimuth resolution and range resolution can be obtained from:

$$\theta_a = \frac{\lambda_c}{L_{\text{eff}}} \quad \delta_r = \frac{c}{2\text{BW}}, \quad (35)$$

where λ_c is the wavelength of the center frequency and L_{eff} denotes the effective size of the aperture. For the antenna we used in the simulation, the azimuth resolution is 1.7° , and the range resolution is 2.3 cm.

The imaging scene is discretized into a dense grid with range and azimuth dimensions, and the scattering coefficient of the targets obeys $\mathcal{CN}(0,1)$. All the simulations are processed in the MATLAB environment and on a computer with an Intel Xeon CPU and 6 GB RAM.

The results of sliding-window IFFT processing with randomly chosen azimuth field data are shown in Fig. 4(b). The length of window P is set as 16 experimentally, as well as the number of frequencies.

The first imaging scene has three scatters located in the same range but different azimuth angles. The measurement vector \mathbf{g} can be calculated according to equation (18). Then we perform \mathbf{g} with sliding-window IFFT, as shown in Fig. 4 (b). The length of the window is P , and the corresponding subband width is $B_\Delta = (P-1)\Delta f$. The range resolution of results is given by $\Delta R = c/2B_\Delta$. The maximum column of results corresponds to the new measurement vector Ψ . According to the index of maxima, the range of interest is [4.34, 5.54] m. The IFFT results with respect to \mathbf{g} are shown in Fig. 4 (c). We can reduce ROI to [4.48, 4.52] m, and reconstruction areas are limited to a very narrow band. Then, we update the measurement matrix Φ by using the inner product of the corresponding Fourier coefficients and constrained measurement matrix \mathbf{H}_{ROI} .

Since the updated measurement matrix Φ is still underdetermined, we need a compress sensing reconstruction algorithm to solve the modified equation. Here, the orthogonal matching pursuit algorithm is employed to retrieve the scene. The reconstructed reflectivity coefficients of σ_{R2} are shown in Fig. 4 (d). It is obvious that all three scatters are preserved clearly. Moreover, to compare the performance of the proposed method with that of existing algorithms, we reconstruct the scene with the algorithm in [30], as shown in Fig. 4 (e), and the brute force method, which uses the ensemble

measurement matrix directly, as shown in Fig. 4 (f). We can see that in both images, all three scatters are well estimated. However, the consumed times in Fig. 4 (d), (e) and (f) are 0.35 s, 2.7 s and 9.4 s, respectively. Hence the acceleration ratio of the proposed fast range decoupling algorithm is calculated to be 26.8, while that of the algorithm in [30] is 3.5.

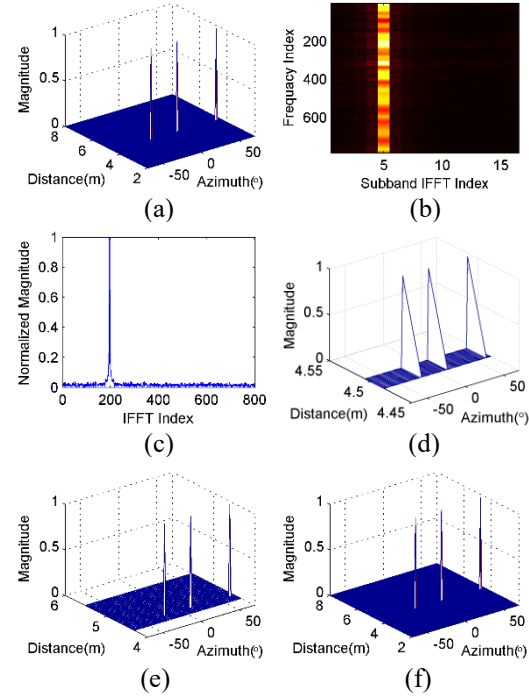


Fig. 4. 2D scene imaging results with 3 point-like scatters. (a) True scene with 3 scatters located in the range of approximately 4.5 m. (b) Result of slight-windowed IFFT with respect to \mathbf{g} with a window length of 16. (c) Results of IFFT operation with respect to \mathbf{g} with all frequency points. (d) Images obtained with proposed method. (e) Images obtained with method of [30]. (h) Image obtained by ensemble H corresponding to [2,8] m.

For the problem of that targets located in far more range cells in scenes, the scale of the measurement matrix would increase rapidly. It is seen from Fig. 5 (a) that targets lie in the range of around 4.5 and 6.9 m from the antenna panel, and the entire range area is [2,8] m. The result of the sliding-windowed IFFT to the received data \mathbf{g} is plotted in Fig. 5 (b). We can see from Fig. 5 (b) that the targets are well separated in two different range cells. Fig. 5 (c) shows the IFFT results to \mathbf{g} with all frequency points, and the size of the ROI could be slumped. Then the modified measurement equation corresponding to each ROI could be built and the reconstruction results are shown in Fig. 5 (d) and Fig. 5 (e). We can observe that the scatters at different locations are estimated accurately.

Similarly, we reconstruct the scene with the algorithm in [30], as shown in Fig. 5 (f) and Fig. 5 (g), and the brute force method, as shown in Fig. 5 (h). The consumed times in Figs. 5 (d)-(h) are 0.32 s, 0.26 s, 3.76 s, 3.70 s and 9.61 s, respectively. Since the reconstruction could be processed in parallel, the acceleration ratio of the proposed method can be calculated to be 30, while that of the algorithm in [30] is 2.6. The imaging efficiency is enhanced obviously.

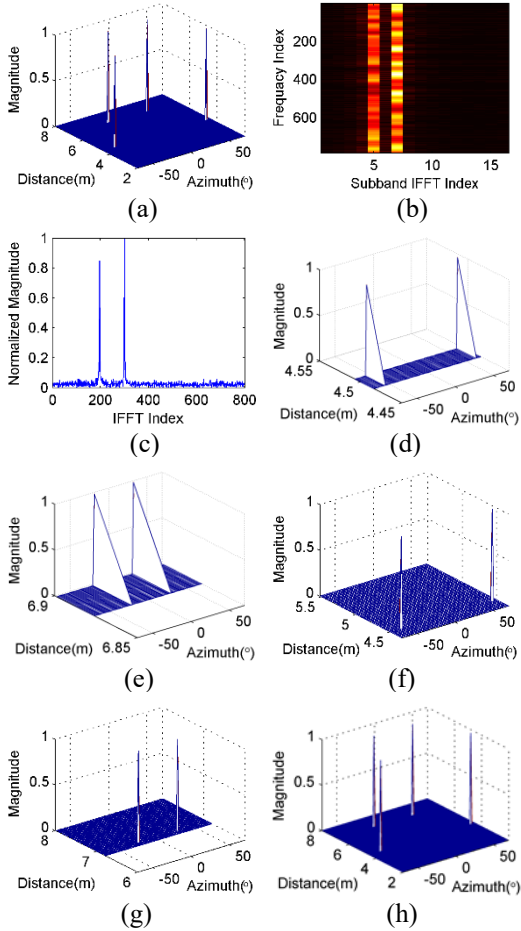


Fig. 5. 2D scene imaging results with scatterers located at different range positions. (a) True scene with 4 point-like scatterers located in the range of approximately 4.5 m and 6.9 m. (b) Result of slight-windowed IFFT with respect to \mathbf{g} with a window length of 16. (c) Result of IFFT operation with respect of \mathbf{g} . (d), (e) Images obtained with the proposed method. (f), (g) Images obtained with the method of [30]. (h) Is an image obtained by ensemble H corresponding to [2,8] m.

Let us analyze the computational complexity of the proposed algorithm. The reconstructed approach employed in this paper is the OMP algorithm, whose computational complexity is $O(LMN)$ [34],[35]. L is

the number of iterations, M is the number of frequency points, and N is the number of unknown voxels in the ROI. It should be noted that $L < M \ll N$. The computational cost of the proposed algorithm is mainly from step 3 to step 6 of the summarization. Assuming that the length of the sliding window is m , then the scene could be decomposed to m range cells. In step 3, the cost of IFFT operations is $O(m \log(m))$. K denotes the number of IFFT operation, given by $K = M - m + 1$. Then, the total computation cost is $O(Km \log(m))$. In step 4, the computational cost is $O(M \log(M))$. Define n as the \mathbf{R}_1 to \mathbf{R}_2 ratio. The computational cost of calculating measurement matrix Φ is $K \times \frac{N}{mn} \times m \log(m) =$

$$\frac{KN}{n} \log(m) \text{ in step 5. In step 6, since the different range cells could be processed in parallel, the computational cost is } O(LKN/mn). \text{ Therefore, the total computational cost of the proposed algorithm is:}$$

$$O(Km \log(m) + M \log(M) + K \frac{N}{n} \log(m) + LK \frac{N}{mn}). \quad (36)$$

Although the computational complexities of both the proposed algorithm and the brute force method are $O(N)$, the memory requirements of our approach for calculating and storing the measurement matrix are decreased sharply. The cost reduction benefits from the sharp drop of the ROI and the parallel processing of partitioned range cells. Furthermore, considering the high dimensionality feature of imaging information, the total computational costs are lowered significantly.

VI. CONCLUSIONS

In this paper, we propose a fast range decoupling algorithm that can reconstruct the partitioned range area in real-time. This proposed algorithm has a lower computational cost and a higher imaging efficiency, due to the ROI reduction and the parallel way of reconstructing the scene. Moreover, the method could produce real-time images of far-field scenes. Further research will concentrate on improving the algorithm in practical applications.

ACKNOWLEDGMENT

We would like to thank Dr. Guy Lipworth and Center for Metamaterials and Integrated Plasmonics, Duke University for providing us the data.

REFERENCES

- [1] J. A. Ribeiro, C. M. Pereira, A. F. Silva, and M. G. F. Sales, "Disposable electrochemical detection of breast cancer tumour marker CA 15-3 using poly (Toluidine Blue) as imprinted polymer receptor," *Biosensors and Bioelectronics*, vol. 109, pp. 246-

- 254, June 2018.
- [2] S. S. Gorthi, D. Schaak, and E. Schonbrun, "Fluorescence imaging of flowing cells using a temporally coded excitation," *Opt. Exp.*, vol. 21, no. 4, pp. 5164-5170, Feb. 2013.
- [3] X. Zhuge and A. G. Yarovoy, "A sparse aperture MIMO-SAR-based UWB imaging system for concealed weapon detection," *IEEE Transactions on Geoscience and Remote Sensing*, vol. 49, no. 1, pp. 509-518, July 2011.
- [4] U. Alkus, A. B. Sahin, and H. Altan, "Stand-off through-the-wall W-band millimeter-wave imaging using compressive sensing," *IEEE Geoscience and Remote Sensing Letters*, vol. 15, no. 7, pp. 1025-1029, Apr. 2018.
- [5] Y. Gao, W. Peng, Y. Qu, and J. Ding, "Through-the-wall imaging based on modified compressive sampling matching pursuit," *2017 Sixth Asia-Pacific Conference on Antennas and Propagation (APCAP)*, Xi'an, China, pp. 1-3, Oct. 2017.
- [6] J. Hunt, T. Driscoll, A. Mrozack, G. Lipworth, M. Reynolds, D. Brady, and D. Smith, "Metamaterial apertures for computational imaging," *Science*, vol. 339, no. 6117, pp. 310-313, Jan. 2013.
- [7] J. Hunt, J. Gollub, T. Driscoll, G. Lipworth, A. Mrozack, M. Reynolds, D. Brady, and D. Smith, "Metamaterial microwave holographic imaging system," *J. Opt. Soc. Amer. A, Opt. Image Sci.*, vol. 31, no. 10, pp. 2109-2119, Oct. 2014.
- [8] J. Gollub, O. Yurduseven, K. P. Trofatter, D. Arnitz, M. F. Imani, T. Sleasman, M. Boyarsky, A. Rose, A. Pedross-Engel, H. Odabasi and T. Zvolensky, "Large metasurface aperture for millimeter wave computational imaging at the human-scale," *Scientific Reports*, vol. 7, no. 1, pp. 1-9, Feb. 2017.
- [9] G. Lipworth, A. Mrozack, J. Hunt, D. L. Marks, T. Driscoll, D. Brady, and D. R. Smith, "Metamaterial apertures for coherent computational imaging on the physical layer," *J. Opt. Soc. Amer. A, Opt. Image Sci.*, vol. 30, no. 8, pp. 1603-1612, Aug. 2013.
- [10] G. Lipworth, A. Rose, O. Yurduseven, V. R. Gowda, M. F. Imani, H. Odabasi, P. Trofatter, J. Gollub, and D. R. Smith, "Comprehensive simulation platform for a metamaterial imaging system," *Appl. Opt.*, vol. 54, no. 31, pp. 9343-9353, Nov. 2015.
- [11] G. Lipworth, J. Hunt, A. Mrozack, D. Brady, and D. R. Smith, "Simulations of 2D metamaterial apertures for coherent computational imaging," *2013 IEEE International Conference on Microwaves, Communications, Antennas and Electronic Systems (COM-CAS 2013)*, Tel Aviv, Israel, pp. 1-4, Oct. 2013.
- [12] T. Fromenteze, O. Yurduseven, M. F. Imani, J. Gollub, C. Decroze, D. Carsenat, and D. R. Smith, "Computational imaging using a mode-mixing cavity at microwave frequencies," *Appl. Phys. Lett.*, vol. 106, no. 19, pp. 9343-53, May 2015.
- [13] T. Fromenteze, O. Yurduseven, M. Boyarsky, J. Gollub, D. L. Marks, and D. R. Smith, "Computational polarimetric microwave imaging," *Opt. Exp.*, vol. 25, no. 22, pp. 27488-27505, Oct. 2017.
- [14] D. L. Marks and D. R. Smith, "Mode diversity of weakly modulated cavity antennas," *J. Opt. Soc. Amer. A, Opt. Image Sci.*, vol. 35, no. 1, pp. 135-147, Jan. 2018.
- [15] T. Sleasman, M. F. Imani, J. N. Gollub, and D. R. Smith, "Dynamic metamaterial aperture for microwave imaging," *Appl. Phys. Lett.*, vol. 107, no. 20, pp. 204104, Nov. 2015.
- [16] T. Sleasman, M. Boyarsky, M. F. Imani, J. N. Gollub, and D. R. Smith, "Design considerations for a dynamic metamaterial aperture for computational imaging at microwave frequencies," *J. Opt. Soc. Amer. B, Opt. Phys.*, vol. 33, no. 6, pp. 1098-1111, June 2016.
- [17] A. V. Diebold, M. F. Imani, T. Sleasman, and D. R. Smith, "Phaseless computational ghost imaging at microwave frequencies using a dynamic metasurface aperture," *Appl. Opt.*, vol. 57, no. 9, pp. 2142-2149, Mar. 2018.
- [18] M. F. Imani, T. Sleasman, and D. R. Smith, "Two-dimensional dynamic metasurface apertures for computational microwave imaging," *IEEE Antennas and Wireless Propagation Letters*, vol. 17, no. 12, pp. 2299-2303, Oct. 2018.
- [19] K. Na, L. Li, S. Tian, and Y. Li. "Measurement matrix analysis and radiation improvement of a metamaterial aperture antenna for coherent computational imaging," *Applied Sciences*, vol. 7, no. 9, pp. 933-942, Sep. 2017.
- [20] M. Zhao, S. Zhu, J. Li, H. Shi, J. Chen, Y. He, and A. Zhang, "Frequency-diverse bunching metamaterial antenna for coincidence imaging," *Materials*, vol. 12, no. 11, pp. 1817-1828, Jan. 2019.
- [21] G. Antonini, "Fast multipole formulation for PEEC frequency domain modeling," *Applied Computational Electromag. Society Journal*, vol. 17, no. 3, pp. 1-17, Nov. 2002.
- [22] S. Kahng, "Predicting and mitigating techniques of the PCB rectangular power/ground planes' resonance modes," *Applied Computational Electromagnetics Society Newsletter*, vol. 22, no. 3, pp. 15-23, Nov. 2007.
- [23] S. Patil, M. Y. Koledintseva, and R. W. Schwartz, "Modeling of field distribution and energy storage in diphasic dielectrics," *2006 15th IEEE International Symposium on the Applications of Ferroelectrics*, Sunset Beach, NC, USA, pp. 307-310, July 2006.
- [24] L. Xue and D. Jiao, "Fast and rigorous method for solving low-frequency breakdown in full-wave finite-element-based solution of general lossy problems," *2018 International Applied Computational Electromagnetics Society Symposium (ACES)*, Denver, CO,

USA, pp. 1-2, Mar. 2018.

- [25] F. Feng, C. Zhang, J. Ma, and Q. Zhang, "Parametric modeling of EM behavior of microwave components using combined neural networks and pole-residue-based transfer functions," *IEEE Transactions on Microwave Theory and Techniques*, vol. 64, no. 1, pp. 60-77, Jan. 2016.
- [26] N. Calik, M. A. Belen, P. Mahouti, and S. Koziel, "Accurate modeling of frequency selective surfaces using fully-connected regression model with automated architecture determination and parameter selection based on Bayesian optimization," *IEEE Access*, vol. 9, pp. 38396-38410, Mar. 2021.
- [27] O. Yurduseven, J. N. Gollub, A. Rose, D. L. Marks, and D. R. Smith, "Design and simulation of a frequency-diverse aperture for imaging of human-scale targets," *IEEE Access*, vol. 4, pp. 5436-5451, July 2016.
- [28] D. L. Marks, O. Yurduseven, and D. R. Smith, "Fourier accelerated multistatic imaging: A fast reconstruction algorithm for multiple-input multiple-output radar imaging," *IEEE Access*, vol. 5, pp. 1796-1809, Feb. 2017.
- [29] C. G. Walter, R. M. Majewski, and R. S. Goodman, *Spotlight Synthetic Aperture Radar: Signal Processing Algorithms*. Boston, MA, USA: Artech House, 1995.
- [30] Z. Wu, L. Zhang, H. Liu, and N. Kou, "Range decoupling algorithm for accelerating metamaterial apertures-based computational imaging," *IEEE Sensors Journal*, vol. 18, no. 9, pp. 3619-3631, Mar. 2018.
- [31] L. Mandel and E. Wolf, *Optical Coherence and Quantum Optics*. Cambridge University, 1995.
- [32] J. W. Goodman, *Introduction to Fourier Optics*. 3rd ed., Englewood, CO, USA: Roberts and Company, 2005.
- [33] F. C. Lin and M. A. Fiddy, "Image estimation from scattered field data," *Int. J. Imag. Syst. Technol.*, vol. 2, no. 2, pp. 76-95, June 1990.
- [34] B. L. Sturm and M. G. Christensen, "Comparison of orthogonal matching pursuit implementations," *2012 Proceedings of the 20th European Signal Processing Conference (EUSIPCO)*, Bucharest, Romania, pp. 220-224, Oct. 2012.
- [35] S. Hsieh, C. Lu, and S. Pei, "Fast OMP: Reformulating OMP via iteratively refining ℓ_2 -norm solutions," *2012 IEEE Statistical Signal Processing Workshop (SSP)*, Ann Arbor, MI, USA, pp. 189-192, Aug. 2012.



Yuteng Gao was born in Shannxi Province, China, in 1988. He received the B.S. and M.S. degree in School of Electronics and Information, Northwestern Polytechnical University in Xi'an City, China, in 2010 and 2013 respectively. He is presently working on his Ph.D. degree in School of Electronics and Information, Northwestern Polytechnical University in Xi'an City, China. His research interests include millimeter wave, antenna design and radar imaging.



Wencan Peng was born in Hubei Province, China, in 1987. She received the B.S. degree in School of Measuring and Optical Engineering, Nanchang Hangkong University in Nanchang City, China, in 2010. Then, she received the M.S. and Ph.D. degree in School of Electronics and Information, Northwestern Polytechnical University in Xi'an City, China, in 2013 and 2020 respectively. Now, she is working with Payload Research Center, Academy of Space Information System (CASC Xi'an). Her research interests include: array signal processing and array calibration.



Min Wang (IEEE Member), received the B.S. degree from Xidian Univ. China in 2000; M.S. and Ph.D. degrees in Signal and Information Processing from Xidian Univ., Xi'an China, in 2003 and 2005 respectively. He is working with National Lab of Radar Signal Processing in Xidian University. His research interests include sparse signal processing, millimeter wave/Terahertz radar and high resolution radar imaging.



Chenjiang Guo was born in Shannxi Province, China, in 1963. CIE Senior Member, Antenna Society Committee Member. He received the B.S., M.S. and Ph.D. in School of Electronics and Information, Northwestern Polytechnical University in Xi'an City, China, in 1984, 1987 and 2007 respectively. He is a Professor in School of Electronics and

Information NWPU. His research interests include: array signal processing, theory and design of antenna.



Jun Ding, received her B.Eng. degree in Electronic Engineering in 1986 from Northwestern Polytechnical University (NWPU). She obtained her M.S. degree in Electromagnetic Fields and Microwave Techniques in 1989 from the NWPU. In 2005, she received her Ph.D. degree in Circuits and Systems from the NWPU. She is now a Professor of Electromagnetic Fields and Microwave Techniques in the NWPU. Her research interests include electromagnetic calculation, antenna theory and design, microwave circuit design, and electromagnetic compatibility (EMC).